THE ASTROPHYSICAL JOURNAL, 495:297–308, 1998 March 1

A PRESCRIPTION FOR BUILDING THE MILKY WAY'S HALO FROM DISRUPTED SATELLITES

KATHRYN V. JOHNSTON
Institute for Advanced Study, Olden Lane, Princeton, NJ 08540; kvj@sns.ias.edu

Received 1997 June 6; accepted 1997 October 10

ABSTRACT

We develop a semianalytic method for determining the phase-space population of tidal debris along the orbit of a disrupting satellite galaxy and illustrate its use with a number of applications.

We use this method to analyze Zhao's proposal that the microlensing events toward the Large Magellanic Cloud (LMC) might be explained by an appropriately placed tidal streamer and find that his scenarios lead either to unacceptably high overdensities (10%–100%) in faint star counts (apparent magnitudes 17.5–20.5) away from the Galactic plane or short timescales for the debris to disperse (10^8 yr).

We predict that the tidal streamers from the LMC and the Sagittarius dwarf galaxy currently extend over more than 2π in azimuth along their orbits. Assuming that each satellite has lost one-half of its primordial mass, we find that the streamers will have overdensities in faint star counts of 10%–100% and less than 1%, respectively, and conclude that this mass-loss rate is unlikely for the LMC but possible for Sagittarius. If the Galaxy has accreted 100 objects of 10^5–10^6 $M_\odot$ (comparable to its current population of globular clusters) at distances of 20–100 kpc during its lifetime, then 10% of the sky will now be covered by tidal streamers.

Subject headings: galaxies: interactions — Galaxy: evolution — Galaxy: formation — Galaxy: halo — Galaxy: kinematics and dynamics — Magellanic Clouds

1. INTRODUCTION

Two fundamental astrophysical questions that can be addressed with Galactic research are, How are galaxies formed? and What are they made from? If galaxies formed hierarchically, we expect satellite accretion to have played some role in Galactic history and might hope to address the former question by searching for signatures of these events. The latter question is currently being addressed by microlensing surveys of the Galactic halo (e.g., Alcock et al. 1996). In most models for the currently available microlensing results, it is assumed that the halo is sufficiently smooth for its global baryonic population to be determined from a local sample. Metcalf & Silk (1996) and Zhao (1997) have pointed out that lumps in the halo, caused by either dark clusters or debris from satellite disruption, would jeopardize this interpretation.

To address both of these questions, therefore, we need to quantify the significance of the presence of accreted structure in the Galactic halo. Unavane, Wyse, & Gilmore (1996) looked at the distribution of halo stars in age and metallicity and concluded that no more than 10% of these stars could have been accreted from the destruction of galaxies with stellar populations like those of the dwarf spheroidal satellites of the Milky Way. An alternative approach, which requires no assumptions about the age or metallicity of stars in accreted satellites, is to look for signatures of accretion in the kinematic and spatial distribution of the halo.

Numerical simulations have confirmed the physical intuition that lumps observed in the halo's phase-space distribution could be associated with accretion events. They have shown that an initially spherical satellite will become distorted when introduced into a tidal field, with stripped stars forming long streams along its orbit, both ahead and behind (see, e.g., McGlynn 1990; Moore & Davis 1994; Oh, Lin, & Aarseth 1995; Piatek & Pryor 1995; Velazquez & White 1995; Johnston, Spergel, & Hernquist 1995; Johnston, Hernquist, & Bolte 1996, hereafter JHB; Kroupa 1997). Analyses of the tidal debris in these simulations have demonstrated that these star streams can maintain coherence for the lifetime of the Galaxy and that long-lived moving groups of stars are a natural consequence of tidal disruption (Johnston et al. 1995; JHB).

There is increasing evidence of morphological distortions, reminiscent of these simulations, in the Milky Way's satellites: surface density contours of the Sagittarius dwarf galaxy (discovered by Ibata, Gilmore, & Irwin 1994) have now been reported to cover an angular region 8×22 deg^2 (Mateo et al. 1996; Alard 1996; Fahlman et al. 1996; Ibata et al. 1997), distorted isophotes have been seen in several globular clusters (Grillmair et al. 1995), and "extratidal" stars have been discovered in most of the dwarf spheroidal satellites (Gould et al. 1992; Irwin & Hatzidimitriou 1995; Kuhn, Smith, & Hawley 1996).

Substructure in the spatial distribution of the Milky Way's dwarf spheroidal satellites, in the form of alignments along great circles, has also historically been attributed to the ancient disruption of a much larger body (Lynden-Bell 1976; Kunkel & Demers 1977), and further possible associations among the halo's globular cluster population have recently been found (Lin & Richer 1992; Majewski 1994; Fusi-Pecci et al. 1995; Lynden-Bell & Lynden-Bell 1995).

In the stellar halo, the advent of various digitized plate surveys (e.g., Maddox et al. 1990; Pennington et al. 1993; Weir, Fayyad, & Djorgovski 1995) raises the possibility of searching for lumps in its projected angular distribution: the dwarf spheroidal galaxy Sextans was found as a simple overdensity in star counts from Automated Plate Measuring (APM) machine scans of UK Schmidt plates (Irwin et al. 1990); Klenya et al. (1997) have developed a circular filter technique that can be used to search for systems with similar morphologies and produce a quantitative estimate of the completeness of the sample that has been found; and, motivated by the work on satellite alignments, JHB proposed the method of great circle cell counts to look for streams of stars along great circles that might result from the disruption of a satellite galaxy.

Observers have been aware of moving groups as distinct lumps in the local stellar phase-space distribution for a long time (see, e.g., Eggen 1965), and similar structures have also now been reported in the halo (see, e.g., Sommer-Larsen & Christiansen 1987; Arnold & Gilmore 1992; Majewski, Munn, & Hawley 1994, 1996; for a comprehensive review of this subject see Majewski, Hawley, & Munn 1996). These discoveries are currently being followed up with systematic spatial and kinematic surveys of larger portions of the halo with the hope of assessing how exceptional this substructure is (S. R. Majewski 1997, private communication).

Overall, the qualitative comparison of numerical and observational work outlined above clearly demonstrates that satellite accretion is ongoing in the Milky Way and is likely to have occurred often in the past. To address the aim of quantifying the presence of accreted structure, the characteristics of a specific phase-space feature (such as a moving group) or the frequency with which such features are found in the stellar halo could be interpreted using a suite of N-body simulations. However, the number of accretion events that such a study can survey is limited by time and computational cost considerations. An alternative approach was adopted by Tremaine (1993), who restricted the description of a trail to simple estimates for its length and width given the parent satellite's mass and distance from the Galactic center. This allowed him to derive analytic expressions for the fractional sky coverage of tidal debris from an ensemble of satellites but at the expense of a more precise knowledge of the structure of the individual trails.

In this paper, we develop a semianalytic technique for finding the density distribution along the entire length of a debris trail, given a satellite of any mass and orbit, assuming only a disruption timescale. This method is complimentary to both previous numerical and analytic work, being less computationally expensive than the former and hence able to cover a wider region of parameter space, while providing a more detailed description of individual trails than the latter. The success of the method is tested through comparison with N-body simulations. As an example of its use, we discuss the implications of this model for the surface density structure of debris trails in the Milky Way system. In a future paper we will extend the technique to generate full phase-space models of halos with a variety of accretion histories and examine their observable properties (Johnston & Majewski 1998).

We present the method in § 2, apply it to the Milky Way system in § 3, and use it to test the plausibility of Zhao's (1997) model of the microlensing results toward the Large Magellanic Cloud (LMC) in § 4. We summarize and discuss the limitations of this approach in § 5. The N-body simulations used to confirm the validity of our technique are outlined in the Appendix.

2. METHOD

In this section we present our method for constructing the phase-space structure along a debris trail. We outline our understanding of the debris's orbital energy distribution, gained from studies of tidally disrupting hydrodynamic systems, in § 2.1. In § 2.2 we apply this picture to find the energy distribution of tidal debris from stellar systems and then convert this to a density distribution along the tidal streamers by using the general properties of orbits in a halo potential. This approach is tested by comparing its predictions with the final particle positions in N-body simulations that have followed satellites evolving in a Milky Way potential for 10 Gyr (see the Appendix). We summarize the technique in § 2.3.

2.1. *Hydrodynamic Systems*

Analytic descriptions of tidal disruption and debris dispersal have been developed for hydrodynamic systems such as planetesimals encountering planets in the solar system (see, e.g., Sridhar & Tremaine 1992) and stars falling into black holes (see, e.g., Evans & Kochanek 1989; Kochanek 1994). In these studies, the satellite is assumed to move on a parabolic orbit, with internal properties such that it disrupts at pericenter. The size of the satellite as it disrupts is the physical scale where the internal and tidal forces balance—roughly

$$r_{\text{tide}} = \left(\frac{m}{M}\right)^{1/3} R\,, \tag{1}$$

where m is the mass of the satellite system, R is the distance of closest approach between the parent and satellite, and M is the mass of the parent system (see Roche 1847). The typical scale of the energy distribution of the debris is then the change in the Keplerian potential energy on this spatial scale,

$$\epsilon_{\text{Kepler}} = r_{\text{tide}} \frac{d\Phi}{dR} = \left(\frac{m}{M}\right)^{1/3} \frac{GM}{R}\,. \tag{2}$$

This energy scale lies between the orbital energy, $\epsilon_{\text{orb}} = GM/R = (M/m)^{1/3}\epsilon_{\text{Kepler}}$, and the internal energy of the satellite, $\epsilon_{\text{int}} = Gm/r = (m/M)^{2/3}\epsilon_{\text{Kepler}}$. Thus, in the regime typically considered, where $(m/M)^{1/3} \ll 1$, the debris from a disruption event occupies a region in energy space where the perturbation from the satellite's original orbital energy is small compared to ϵ_{orb} but large compared to ϵ_{int}.

Indeed, Sridhar & Tremaine (1992) and Evans & Kochanek (1989) both found the energy distribution of the debris to be continuous over a finite range, with scale ϵ_{Kepler}, centered on the initial orbital energy. Approximately one-half of the material moved to unbound, hyperbolic orbits, and one-half moved to bound elliptic orbits. Ignoring the influences of self-gravity and fluid effects, the subsequent evolution of the debris could be followed analytically by simply mapping the distribution in energy to one in orbital time periods.

2.2. *Stellar Systems*

The same physical principles used to determine the energy distribution and dispersal of tidal debris for hydrodynamic systems apply to stellar systems, but the theory is less complex since it involves only collisionless particle dynamics. Its application to Galactic satellites differs in two ways: (1) the parent potential is not Keplerian, and (2) the satellite undergoes repeated encounters. Mass is lost continuously but predominantly during the pericentric passages (see, e.g., Fig. 2 of JHB). The implications of these differences are outlined in §§ 2.2.1 and 2.2.2, and the resulting prediction for the matter distribution along a tidal streamer is presented in § 2.2.3. The effect of the omission of self-gravity from this analysis is discussed in § 2.2.4.

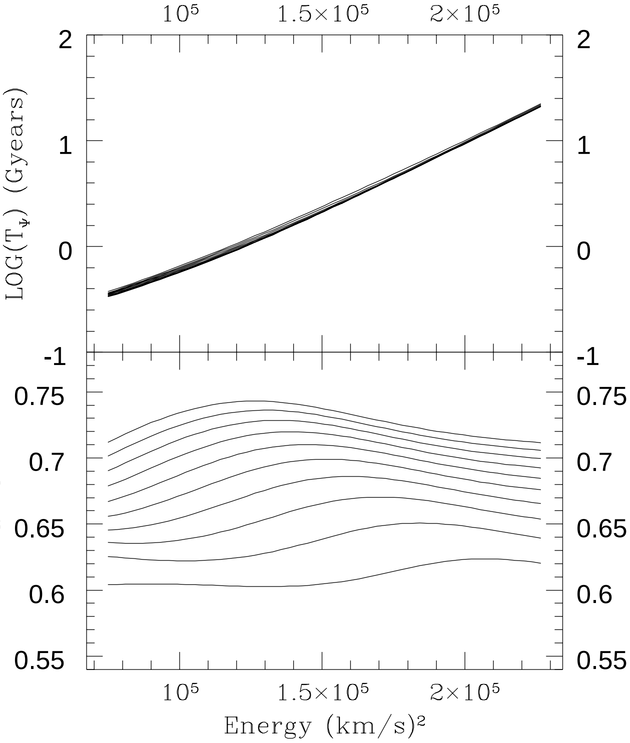

FIG. 1.—Azimuthal time period, T_Ψ, as a function of energy for orbits with angular momentum, $J/J_{\rm circ} = 0.05 - 1.0$, in the spherical Milky Way potential, $\Phi_{\rm MW}$ (eq. [A1]) (*upper panel*) and the ratio of radial to azimuthal time periods, T_R/T_Ψ, as a function of energy (*lower panel*).

2.2.1. *Orbits in a Halo Potential*

Orbits in a spherical potential can be classified by their energy, E, and angular momentum, J, which completely specify their planar paths (R, Ψ) in polar coordinates in the orbital plane as well as their radial and azimuthal time periods (T_R, T_Ψ). Hence, for the purpose of characterizing the properties of orbits in the halo, we consider a spherical approximation to the full Galactic potential that is used in the numerical simulations (see the Appendix). This potential, $\Phi_{\rm MW}$, is constructed from bulge and halo components taken directly from equation (A1) and a third spherical component, $\Phi = -GM_{\rm disk}/(R^2 + a^2)^{1/2}$, with the mass and scale length of the disk given in equation (A1).

For this spherical potential, the extent of the energy distribution in the debris from a satellite on orbit with pericenter R_p can be found analytically by using generalized forms of equations (1) and (2):

$$r_{\rm tide} = \left(\frac{m}{M_p}\right)^{1/3} R_p \,, \tag{3}$$

$$\epsilon_\Phi = r_{\rm tide}\,\frac{d\Phi}{dR} = \left(\frac{m}{M_p}\right)^{1/3} R_p\,\frac{d\Phi}{dR} = (GmR_p)^{1/3}\left(\frac{d\Phi}{dR}\right)^{2/3} , \tag{4}$$

where $M_p = R_p^2(d\Phi/dR)/G$ is the mass of the Galaxy within R_p.[1] However, the azimuthal and radial orbital time periods must be found numerically.

The upper panel of Figure 1 shows T_Ψ as a function of E for $J/J_{\rm circ} = 0.05, 0.1, 0.15, \ldots, 1.0$ (where $J_{\rm circ}$ is the angular momentum of a circular orbit). Note that the lines in this panel are almost indistinguishable, as T_Ψ depends only very weakly on J. For a circular orbit, T_Ψ can be calculated exactly:

$$T_\Psi^{\rm circ} = 2\pi\sqrt{\frac{R}{(d\Phi/dR)}} \,. \tag{5}$$

The solid lines in the lower panel of Figure 1 show the ratio T_R/T_Ψ for the same values of $J/J_{\rm circ}$. For a near-circular orbit, T_R was calculated using the epicyclic approximation (see Binney & Tremaine 1987):

$$T_R^{\rm circ} = \frac{2\pi}{\kappa} \,, \quad \kappa^2 = \frac{d^2\Phi}{dR^2} + \frac{3J_{\rm circ}}{R^4} = \frac{d^2\Phi}{dR^2} + \frac{3}{R}\frac{d\Phi}{dR} \,. \tag{6}$$

For a radial orbit, $T_R/T_\Psi = \frac{1}{2}$.

Since we are primarily interested in the construction of the outer halo (greater than 20 kpc) from tidal debris, we might hope to represent the full Milky Way potential as logarithmic in this region,

$$ {}_{\log} = v_{\rm circ}^2 \log\,(R/R_0) \,, \quad v_{\rm circ} = 200 \text{ km s}^{-1} \,,$$

$$R_0 = \text{arbitrary constant} \,. \tag{7}$$

(The IAU standard for the circular velocity at the solar radius is $v_0 = 220$ km s^{-1}, but recent estimates tend to be lower than this—see Sackett 1997 for a summary.) This further approximation is not strictly necessary, but it allows us to express equations (4), (5), and (6) in simple form:

$$\epsilon_{\log} = \left(\frac{Gm}{R_p}\right)^{1/3} (v_{\rm circ}^2)^{2/3} \,, \tag{8}$$

$$T_\Psi^{\rm circ} = \frac{2\pi}{v_{\rm circ}}\,R_{\rm circ} = \frac{2\pi R_0}{v_{\rm circ}} \exp\left(\frac{E - v_{\rm circ}^2/2}{v_{\rm circ}^2}\right)$$

$$= 1.5 \times \left(\frac{R_{\rm circ}}{50 \text{ kpc}}\right) \text{Gyr} \,, \tag{9}$$

$$\frac{T_R^{\rm circ}}{T_\Psi^{\rm circ}} = \sqrt{\frac{1}{2}} \,. \tag{10}$$

In Figure 2 we make some assessment of how successful this representation is for our own three-component model of the Milky Way. The dotted line shows $(\epsilon_{\log}/\epsilon_{\rm MW} - 1)$ as a function of R_p, and the solid line shows $(T_{\log}/T_{\rm MW} - 1)$ for time periods of circular orbits as a function of $R_{\rm circ}$, where "log" and "MW" denote quantities calculated in the potentials $\Phi_{\log}$ and $\Phi_{\rm MW}$, respectively. The figure demonstrates that these properties in the two potentials differ by only 10% in the region of interest.

We use Figures 1 and 2 to justify the following approximations:

1. We use the logarithmic potential to estimate the scale of the energy distribution (eq. [8]).
2. We assume that the azimuthal time period, T_Ψ, of an orbit is a function only of its energy, independent of its angular momentum or eccentricity. We calculate T_Ψ using the expression for a circular orbit of energy E in a logarithmic potential given by equation (9). This allows us to write down the relation between T_Ψ for orbits of energy E and $(E + \Delta E)$ as

$$T_\Psi(E + \Delta E) = \tau(\Delta E)T_\Psi(E) \,, \quad \tau(\Delta E) = \exp\left(\frac{\Delta E}{v_{\rm circ}^2}\right) . \tag{11}$$

---

[1] In a calculation analogous to Roche's (1847) work, King (1962) found the limiting radius of a star cluster on an orbit of eccentricity, e, and pericenter, R_p, to be $r_{\rm tide} = R_p[m/M(3 + e)]^{1/3}$.

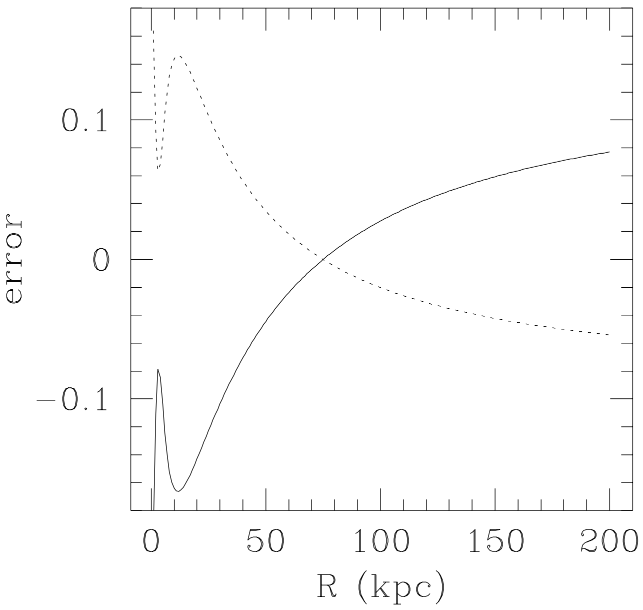

FIG. 2.—The fractional error in the calculation of ϵ (*solid line*) (see eq. [8]) and T_Ψ (*dotted line*) if our three-component Milky Way potential (see the Appendix) is approximated as purely logarithmic at all radii.

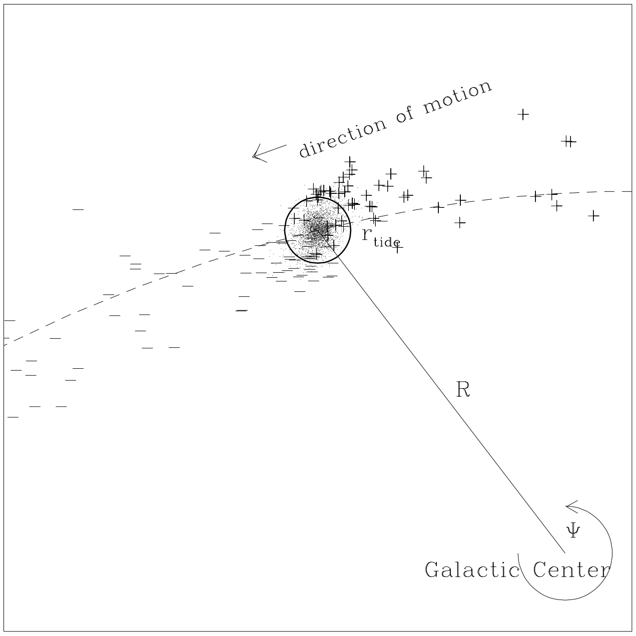

FIG. 3.—Snapshot of particle positions in the orbital plane of a simulation of a tidal encounter. The dots label particles still bound to the satellite, and the minus and plus signs label those unbound on orbits with lower and higher energy than the satellite orbit, respectively. The dashed line shows the satellite's path. The circle shows the physical scale calculated from eq. (3).

3. We take $T_R/T_\Psi = \text{constant} = (1/2)^{1/2}$. Assuming this condition is strictly true, then the angular difference between successive turning points (or pericenters and apocenters) is the same along all orbits. Given the azimuthal time dependence, $\Psi(t)$, of an orbit of energy E and period T_Ψ, we can express the azimuthal path of one with energy $(E + \Delta E)$ and period τT_Ψ as $[\Psi_0 + \Psi(t_0 + t/\tau)]$, where Ψ_0 and t_0 are constants chosen to take into account the difference between the azimuthal and radial phases of the two orbits at $t = 0$.

2.2.2. *Energy Distribution in Debris*

To simplify the calculation of the energy distribution in the tidal streamers, we model the disruption of a satellite as a series of discrete mass-loss events occurring on each pericentric passage (which will clearly be most appropriate for eccentric orbits).

Figure 3 is a "snapshot" from a simulated encounter, showing the positions of particles in the orbital plane of a satellite. The dots show particles still bound to the satellite, and the bold circle shows the extent, $r_{\rm tide}$, from equation (3) that sets the scale of the energy changes. The dashed line shows the satellite's orbit, and the plus and minus signs show unbound particles that have moved to orbits of higher and lower energies, respectively. The plot suggests that mass lost on passages prior to disruption will make two distinct contributions to the energy distribution in the tidal streamers, at positive and negative ΔE, clearly separated from each other in energy by the region where ΔE is too small for a particle to escape from the satellite. In contrast, in their study of hydrodynamic systems disrupting during a single encounter, Evans & Kochanek (1989) found the density of debris to be uniform in energy across the energy scale $\epsilon_{\rm Kepler}$ centered on the satellite's orbit (i.e., $dN/d(\Delta E) = 1/2\epsilon$ for $-\epsilon < \Delta E < \epsilon$). In the light of this study, we expect the particles that become unbound on the final passage, as the satellite disrupts completely, to remain at energies close to the original orbit rather than forming distinct populations at positive and negative ΔE.

To convert these expectations to a formalism for finding the full energy distribution of mass lost from a satellite that disrupts over several orbits, we first define the energy scale of debris lost on the ith of n pericentric passages to be $\epsilon_i = (Gm_i/R_p)^{1/3}(v^2{}_{\rm circ})^{2/3}$, where m_i is the mass still bound to the satellite on that passage (see eq. [8]). Let $N_{\rm peri}(q_i)$ and $N_{\rm disrupt}(q_n)$ be the fractional number densities in scaled energy $q_i = \Delta E/\epsilon_i$ for particles unbound on the ith pericentric passage and as the satellite disrupts, respectively. The full distribution of tidal debris is given by

$$\frac{dN}{d(\Delta E)} = \sum_{i=1,n}\left[\frac{\delta m_i}{m_{\rm debris}}\,\frac{N_{\rm peri}(\Delta E/\epsilon_i)}{\epsilon_i}\right] + \frac{m_n}{m_{\rm debris}}\,\frac{N_{\rm disrupt}(\Delta E/\epsilon_n)}{\epsilon_n}\,, \qquad (12)$$

where $m_{\rm debris}$ is the total mass of the debris, and $\delta m_i = (m_i - m_{i+1})$ is the mass lost on the ith passage.

Figure 4 shows the number density, dN/dq, of unbound particles in scaled energy changes, $q = \Delta E/\epsilon$, at the end of each of the simulations (*histograms*) (see the Appendix), where ϵ is calculated from equation (8) with the values for m and R_p listed in Table 1. As predicted, the debris in all the models covers a similar range in q despite the variety of satellite orbits and masses employed. In the models that were not disrupted during the course of the simulation (models 1, 10, 11, and 12), the debris shows two distinct populations in energy changes, as expected from the discussion above. The other models show similar distributions at lower and higher energies formed at pericentric passages

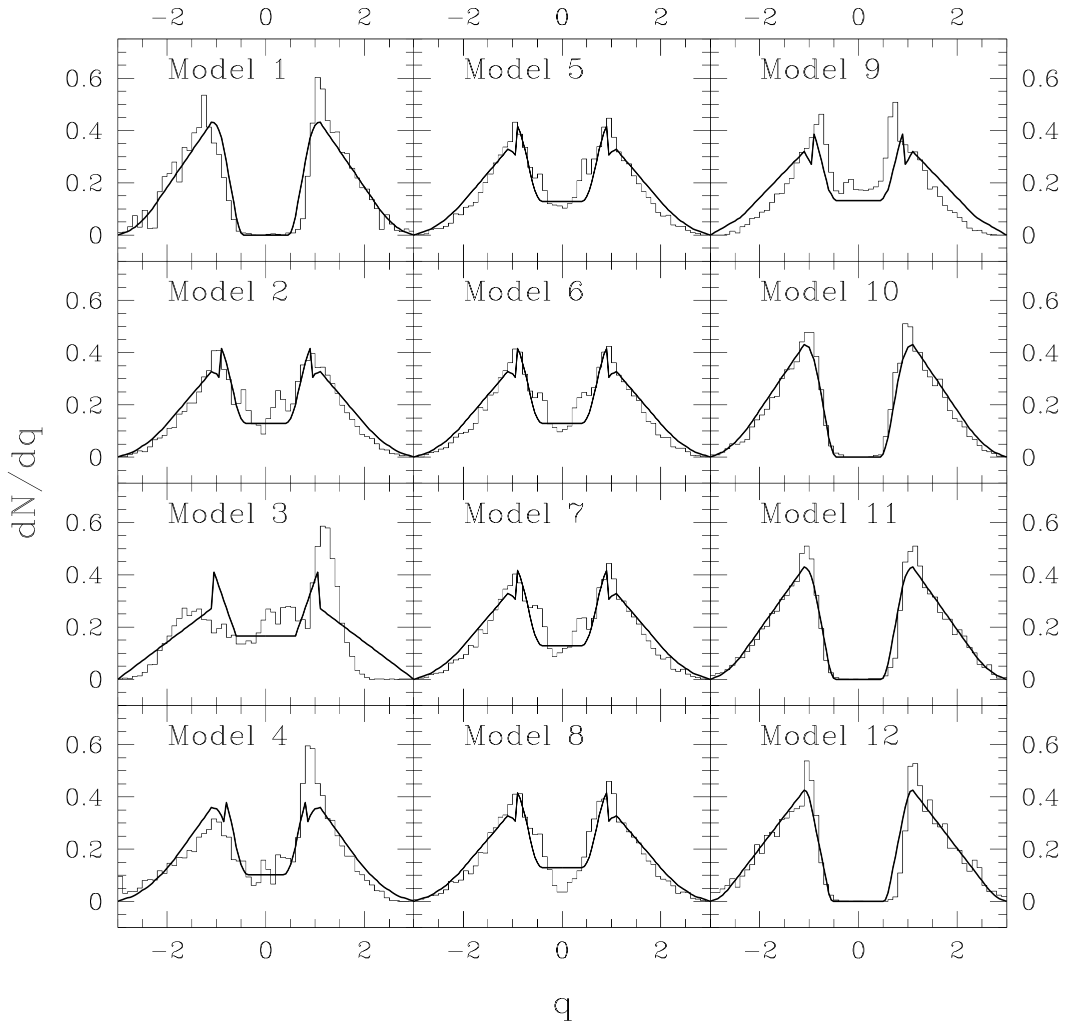

FIG. 4.—Distribution of debris in scaled energy, $q = \Delta E/\epsilon$, at the end of each simulation (*histograms*). The heavy lines show the simple analytic functions that we have used to approximate each of these distributions (see eq. [12]).

prior to the destruction of the satellite, along with a central population of particles with smaller $|\Delta E|$ from the final disruption event. The histograms are similar enough to suggest that we can postulate forms for intrinsic distributions in q for the material torn during each pericentric passage as

$$N_{\mathrm{peri}}(q) = \frac{1}{c-a} \times \begin{cases} (|q| - a)/(b - a)\,, & \text{if } a < |q| < b\,; \\ (c - |q|)/(c - b)\,, & \text{if } b < |q| < c\,; \\ 0\,, & \text{otherwise}\,, \end{cases} \tag{13}$$

and from the satellite disruption as

$$N_{\mathrm{disrupt}}(q) = \frac{1}{2d} \times \begin{cases} 1\,, & \text{if } |q| < d\,; \\ 0\,, & \text{otherwise}\,, \end{cases} \tag{14}$$

where $a = 0.6$, $b = 1.1$, $c = 3.1$, and $d = 1.5$. The shape of these distributions and values for the parameters are chosen by simple inspection of the histograms in Figure 4.

To verify the proposed forms for the scaled energy distributions with each simulation, we need to specify the number of pericentric passages, n, and the mass of the satellite on each passage, m_i, and use these to convert N_{peri} and N_{disrupt} given by equations (13) and (14) to the full distribution in energy changes, $dN/d(\Delta E)$, using equation (12). The mass-loss history—which we characterize by the values of m_i—depends nontrivially on the mass, physical scale, and

TABLE 1

PARAMETERS OF MODELS USED TO GENERATE DEBRIS TRAILS

Model Number	Satellite Mass, m ($M_\odot$)	R_p[a] (kpc)	R_a/R_p[b]	n[c]	f[d]
1	1.0×10^9	39.6	3.4	5	0.18
2	4.1×10^7	43.4	4.0	4	0.30
3	1.9×10^7	45.2	2.4	1	0.65
4	6.9×10^7	26.4	3.0	5	0.30
5	3.3×10^8	43.4	4.0	4	0.30
6	1.2×10^8	43.4	4.0	4	0.30
7	1.4×10^7	43.4	4.0	4	0.30
8	5.1×10^6	43.4	4.0	4	0.30
9	5.8×10^7	43.4	4.0	2	0.50
10	3.3×10^7	43.4	4.0	4	0.25
11	2.9×10^7	43.4	4.0	4	0.20
12	2.4×10^7	43.4	4.0	4	0.12

[a] Pericenter of orbit.

[b] Ratio of apocentric to pericentric distance.

[c] Number of pericentric passages either prior to destruction or during simulation.

[d] Fraction of bound mass lost on each passage.

orbit of the satellite and should be investigated with simulations if a detailed model of a specific tidal disruption event is needed. For our purposes of generating physically reasonable debris trails, we assume that each satellite loses a constant fraction, f, of its remaining mass instantaneously on each passage. To compare with the simulations, we choose f and n to approximate their mass-loss histories by visual inspection of Figure 2 in JHB (see Table 1). Substituting $\delta m_i = f m_i$ and $m_i = (1-f)^i m$ in equation (12), we find the $dN/d(\Delta E)$ plotted as heavy lines in Figure 4. The fits are good enough to justify our use of the simple functional forms for the energy distributions given by equations (13) and (14).

2.2.3. *Matter Distribution along Tidal Streamers*

For any given orbit, with azimuthal time dependence $\Psi(t)$, we can generate a detailed description of the density structure along the tidal streamers at any time by combining the energy distributions and mass-loss histories outlined in § 2.2.2 with the approximations for orbital properties given in § 2.2.1. We assume that particles lost at pericenter initially all have the same radial phase as the satellite. Then the problem of finding the number density of particles at Ψ from mass lost with energy distribution $dN/d(\Delta E)$ during the ith pericentric passage at time t_i reduces to a mapping (using eqs. [8], [11], and [12])

$$\begin{aligned}\frac{dN_i}{d\Psi} &= \frac{dN_i}{d(\Delta E)}\,\frac{d(\Delta E)}{d\tau}\,\frac{d\tau}{d\Psi[t_i+(t-t_i)/\tau]}\\ &= \frac{v_{\rm circ}^2}{\epsilon_i}\,N(q_i)\,\frac{1}{u\dot{\Psi}(t_i+u)}\\ &= \left(\frac{v_{\rm circ}^2}{Gm_i/R_p}\right)^{1/3} N(q_i)\,\frac{1}{u\dot{\Psi}(t_i+u)}\,, \qquad (15)\end{aligned}$$

where $u = (t-t_i)/\tau$, $q_i = \Delta E/\epsilon_i$, and $N(q_i)$ is given by either equation (13) or (14), as appropriate. The complete distribution is calculated by summing over mass lost on each of the pericentric passages.

Figure 5 shows the fraction of unbound particles per degree, $dN/d\Psi$, along the orbit of the satellite at the end of each of the simulations (*histograms*). The heavy lines in the plot are the predictions of the mapping given in equation (15), using the parameters listed in Table 1 and taking $\dot{\Psi}$ to be the angular velocity along the (nonplanar) path of the satellite found by integrating its orbit in the full Milky Way potential given in the Appendix. In general, the semianalytic approach reproduces the density distribution to within a factor of 2 and over 2 orders of magnitude in amplitude.

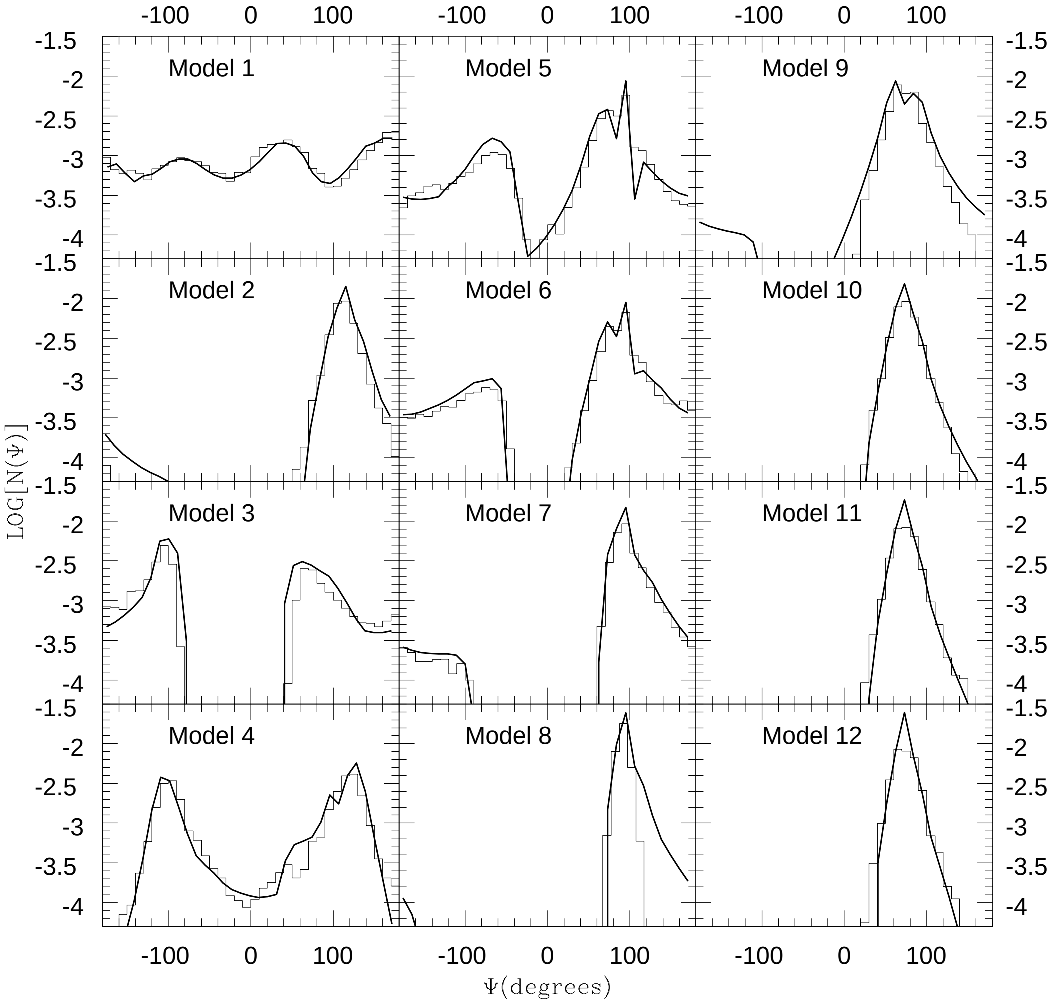

FIG. 5.—Final distribution of debris along orbits for each simulation (*histograms*). The heavy lines are the predictions from eq. (15).

2.2.4. *Self-Gravity in Debris*

The gravitational interactions of particles in the debris trails are neglected in both of the simulations (since the code uses spherical harmonic expansions to evaluate the potential and cannot represent the geometry of the streamers) and the above semianalytic description. However, we can argue that self-gravity is less important than tidal forces for the predicted angular distribution by comparing the influence of the two at each point along the streamers.

Following Roche (1847) and King (1962), we expect the internal and external forces to balance when the debris has a density of order

$$\rho_{\rm crit} = \frac{M(R)}{R^3} \, . \tag{16}$$

The debris density, ρ, can be calculated from equation (15) by including estimates for the stream's angular width, w, and radial extent, ΔR. The former is fixed by the range in orbital inclinations, set at pericenter to

$$w = (r_{\rm tide}/R_p) \, , \tag{17}$$

and the latter is determined by the scale of the energy changes, $\Delta R = \epsilon/(d\Phi/dR) = Rw$ (see eq. [2]). Hence

$$\rho(R, \Psi) = \frac{m_{\rm debris}}{R^2 w \Delta R} \frac{dN}{d\Psi} = \frac{m_{\rm debris}}{R^3} \left(\frac{R_p}{r_{\rm tide}}\right)^2 \frac{dN}{d\Psi} \, . \tag{18}$$

For the center of a disrupting system, the ratio of this density to the critical density for self-gravity to be important is

$$\frac{\rho}{\rho_{\rm crit}} = \frac{R_p}{R} \frac{1}{2d} \frac{1}{t\dot{\Psi}} \tag{19}$$

(combining eqs. [14], [15], [16], and [18]).

This ratio is plotted in Figure 6 for orbits with $J/J_{\rm circ} = 0.28, 0.36, \ldots, 1.0$ (or eccentricities $R_p/R_a \sim 0.07 \ldots 1.0$, where $R_{\rm a}$ is the apocentric distance). At pericenter, the curves reach minima whose amplitudes decrease with J as $\dot{\Psi}(R_p)$ increases. At apocenter, there is a corresponding decrease in $\dot{\Psi}(R_a)$ with J, but this is offset by an increase in the cross-sectional area of the trail because at large distances it is less confined by the tidal field. Thus the density evolution along a circular orbit (*heavy curve*) serves as an upper limit to the behavior along any orbit. Since this never exceeds the critical density, we conclude that our prediction for the matter distribution along the streamers is consistent with the neglect of self-gravity in the analysis. (The density becomes singular as $t \to 0$, since the initial angular extent of the debris in our description is effectively zero at this time.)

Note that mass escaping over the tidal radius of a still-bound satellite will also have density $\lesssim \rho_{\rm crit}$ and is spread over a similar energy scale (see also eqs. [14] and [13]). Hence our neglect of self-gravity is equally valid when modeling the behavior of tidal streamers from Milky Way satellites (such as the LMC).

2.3. *Summary of Technique*

Our method for generating debris distributions along tidal streamers can be summarized as follows:

1. We assume that self-gravity is negligible in the tidal streamers.
2. We apply a simple physical picture to understand the energy scale, ϵ, around the satellite's orbital energy over which the debris is distributed (see §§ 2.1 and 2.2.1 and eq. [8]) and take a functional form for the full distribution in scaled energy changes, $N(\Delta E/\epsilon)$, by examining the results from N-body simulations (see § 2.2.2 and eqs. [13] and [14]).
3. We make the approximation that orbital time periods depend only on their energies. Using this approximation, along with the characteristics of orbits in a purely logarithmic potential (eq. [7]), we relate the energy change, ΔE, to a change in orbital time period (§ 2.2.1 and eq. [11]).
4. We model mass loss as occurring instantaneously at the satellite's pericentric passages and assume that the subsequent turning points along the orbit of the debris and satellite are aligned in azimuth (or T_R/T_Ψ = constant).
5. Combining the above points with the satellite's orbit $[R(t), \Psi(t)]$, we predict the debris distribution along the path of the satellite from mass lost at each previous pericentric passage and sum these to find the full density profile (§§ 2.2.3 and 2.2.4).

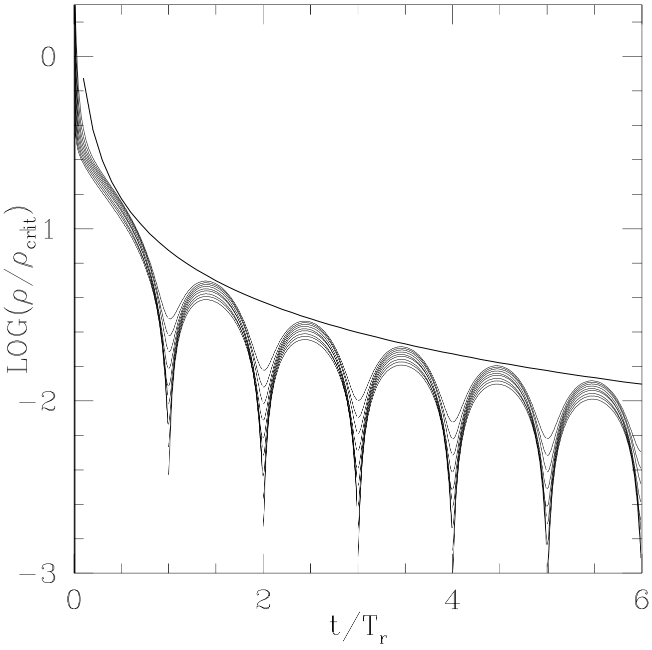

FIG. 6.—Ratio of the density of a remnant following the complete destruction of a satellite to the critical density for self-gravity to be important. The different curves are for orbits with the same energy and $J/J_{\rm circ} = 0.28, 0.36, \ldots, 1.0$ or $R_a/R_p \sim 0.02$–1.0. Pericenter corresponds to the dip in each curve.

3. APPLICATIONS TO THE MILKY WAY SYSTEM

We illustrate some uses of the technique developed in the previous section by asking the following:

Is it possible to detect tidal streamers from any of the Galactic satellites? (§ 3.1)

How long will overdensities in star counts be noticeable following a disruption event? (§ 3.2)

What is the angular scale of a tidal streamer and what fraction of the sky might an ensemble of such streamers cover? (§ 3.3)

3.1. *Should We Expect to See Tidal Streamers from Galactic Satellites?*

If we know the position, radial velocity, and proper motion of a satellite, we can integrate its orbit backward in

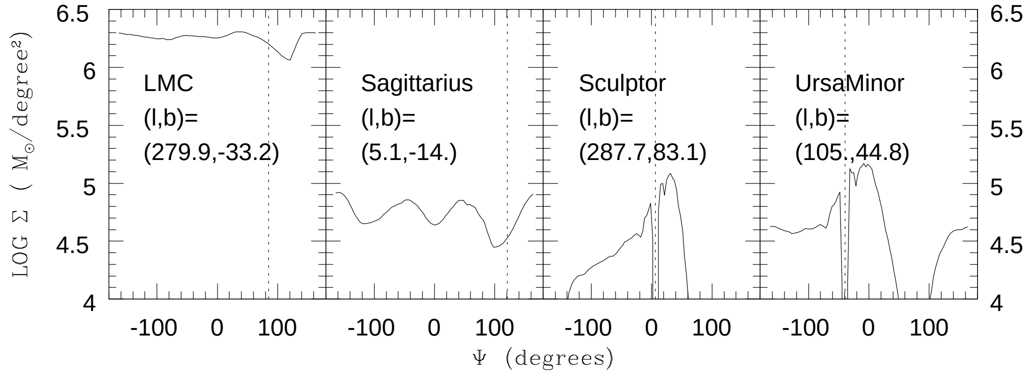

FIG. 7.—Mass surface density distribution for debris along the orbits of those satellites with known proper motions, assuming each has lost one-half of its mass in the last 10 Gyr. The dotted lines show the current position of each satellite. In the right-hand panels, the gap in the surface density at this point is the region that is occupied by particles that are still bound to the satellite. Note that Ψ is measured from the Galactocentric, not heliocentric, position.

time in our (or any other) Milky Way potential to find its angular path, $\Psi(t)$, pericentric position, R_p, and number of encounters, n, in the last 10 Gyr. Assuming the satellite, currently having a mass of $m_{\rm sat}$, has lost mass $m_{\rm debris}$ in this time (or, equivalently, a fraction $f = [m_{\rm debris}/(m_{\rm debris} + m_{\rm sat})]^{1/n}$ of its bound mass on each passage), we can use equation (15) to calculate the matter distribution, $dN/d\Psi$, along the path of the satellite. This can be normalized to give a mass surface density in solar mass per square degree via

$$\Sigma(\Psi) = \frac{m_{\rm debris}}{w}\frac{dN}{d\Psi} = m_{\rm debris}\frac{R_p}{r_{\rm tide}}\frac{dN}{d\Psi}\,, \qquad (20)$$

where w is the width of the debris trail (see eq. [17]). (For simplicity, we have adopted the viewpoint of an observer at the Galactic center in this and all subsequent calculations.)

Figure 7 shows the prediction for Σ along the paths (calculated from their proper motions; see references in Table 2) of the LMC and the Sagittarius, Ursa Minor, and Draco dwarf spheroidals assuming $m_{\rm debris} = m_{\rm sat}$ for each satellite. From estimates for their central luminosity densities and mass-to-light ratios (see, e.g., Irwin & Hatzidimitriou 1995), the central surface densities of these satellites are typically greater than $10^8\ M_\odot\ {\rm deg}^{-2}$. The current position of each satellite is given in Galactic latitude and longitude (l, b), and the corresponding value for the position, Ψ, along the orbit is indicated with the vertical dotted lines. Note that since the extent of the debris's energy distribution is only weakly dependent on the instantaneous mass of the satellite ($\epsilon \propto m_{\rm sat}^{1/3}$), the shape of these curves is nearly independent of $m_{\rm debris}$ so long as $m_{\rm debris} \leq m_{\rm sat}$, and they can be simply scaled down in amplitude for lower mass-loss rates.

Debris from the LMC and Sagittarius spreads over more than 2π in Ψ in 10 Gyr, and in these cases the plot shows the result of summing over all mass that has the same angular phase (i.e., assuming that the orbit is perfectly planar and the same phase corresponds to the same line of sight). Our prediction for the extent of the debris trail from the LMC is consistent with the hypothesis that an ancient accretion event is responsible for the curious alignment of several dwarf spheroidal satellites (Lynden-Bell 1976, 1982), young globular clusters (Lin & Richer 1992; Majewski 1994; Fusi-Pecci et al. 1995), and proper motions of some of these objects (Majewski, Phelps, & Rich 1997) along the great circle defined by the LMC and the Magellanic Stream. This calculation also confirms the idea that a globular cluster that was previously a member of Sagittarius (and several are currently associated with this dwarf—see Da Costa & Armandroff 1995) could now be on the opposite side of the Galaxy (Fusi-Pecci et al. 1995), since the debris is expected to encircle the sky within the lifetime of the Milky Way.

TABLE 2

PARAMETERS OF MILKY WAY SATELLITES

Satelite	Mass ($M_\odot$)	Luminosity, L ($L_\odot$)	R[a,b] (kpc)	R_a/R_p[b,c]	T_Ψ[d] (Gyr)	Debris Scale[e] (width × length, deg)	Proper Motion Reference
LMC	10^{10}	2×10^9	31.9	2.2	1.5	17 × 360	Jones, Klemola, & Lin 1994
Sagittarius	10^8	2×10^7	12.7	3.1	0.7	6 × 360	Irwin et al. 1996
Sculptor	1.4×10^7	1.6×10^6	52.0	2.4	2.6	2 × 36	Schweitzer et al. 1995
Ursa Minor......	3.9×10^7	3.0×10^5	45.7	2.0	2.0	3 × 90	Schweitzer, Cudworth, & Majewski 1998
Draco	5.2×10^7	2.5×10^5	76.0	...	2.6	3 × 60	...
Carina	1.1×10^7	2.9×10^5	89.0	...	3.0	2 × 30	...
Sextans	2.6×10^7	8.3×10^5	91.0	...	3.1	2 × 45	...
Fornax	1.2×10^8	2.5×10^7	133.0	...	4.5	3 × 36	...

NOTE.—The mass, luminosity, and current galactocentric distances are from Jones et al. (1994) (LMC), Ibata et al. (1994) (Sgr), and Mateo et al. (1993) (remaining dwarf spheroidals).

[a] Distance from Galactic center.

[b] The fourth and fifth columns give pericentric distances and time periods integrated in the Galactic potential for those with proper motions. Otherwise, they give the current distance of the satellite and the time period for a circular orbit at that distance.

[c] Ratio of apocentric to pericentric distance.

[d] Azimuthal time period.

[e] Approximate debris scale, calculated from the width and length estimates given by eqs. (17) and (25).

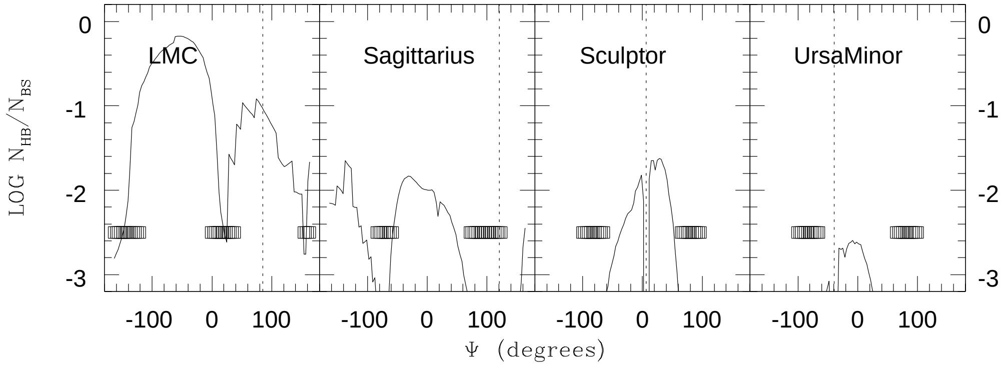

FIG. 8.—Conversion of Fig. 7 to a comparison of the density of horizontal-branch stars, $N_{\rm HB}$, with the background star counts from the Bahcall-Soneira model for the Galaxy, $N_{\rm BS}$. The squares in these panels indicate where the orbit is within 20° of the Galactic disk and where the signature of the debris is most likely to be swamped by foreground objects. The dotted lines show the current position of each satellite. In the right-hand panels, the gap in the surface density at this point is the region that is occupied by particles that are still bound to the satellite.

For any given luminosity function, we can use our estimate for Σ to find the surface density of stars along the trail in apparent magnitude bins. We illustrate this idea by considering horizontal-branch (HB) stars, which we expect to be useful tracers of debris trails. Although not as bright as giant stars, they are easier to distinguish from the foreground disk population using their blue colors. Moreover, we can approximate their absolute magnitudes as

$$M_{\rm HB} = 0.66 + 0.19[{\rm Fe/H}] \qquad (21)$$

(Walker 1992) and therefore find their distances. From equation (21), we know that the apparent magnitudes of HB stars at distances of 25–100 kpc lie in the range 17.5–20.5 mag. In this example, we will ignore any color information and simply contrast their number density along each streamer with star counts at the same Galactic latitude and longitude (l, b) and in the same apparent magnitude range, estimated from the Bahcall-Soneira Galactic model, $N_{\rm BS}$ (Bahcall & Soneira 1980). We convert Figure 7 into an estimate for the number of satellite horizontal-branch stars per square degree via

$$N_{\rm HB} = n_{\rm HB} \frac{L_{\rm sat}}{m_{\rm sat}} \Sigma(\Psi) , \qquad (22)$$

where $n_{\rm HB}$ is the number of horizontal-branch stars per unit luminosity for the satellite's population, and $L_{\rm sat}$ is the total luminosity of the satellite. To estimate a typical value for $n_{\rm HB}$, we note that the observed ratio of the number of HB stars to red giant branch stars with magnitudes less than the horizontal branch lies in the range $n_{\rm HB}/n_{\rm RGB} \sim 1$–2 (Mighell 1990; Buonanno Corsi & Fusi Pecci 1985). Then, using Bergbusch & VandenBerg's (1992) isochrones for an 8.0 Gyr, $[{\rm Fe/H}] = -1.03$ cluster as a representative population, we find $n_{\rm RGB} = 1/528$, which implies $n_{\rm HB} \sim 0.002$–0.004.

In Figure 8 we plot $N_{\rm HB}/N_{\rm BS}$ for $n_{\rm HB} = 0.003$. The squares mark positions along each satellite's orbit that are less than 20° from the Galactic plane, where the background counts are largest. The comparison suggests that even for large mass-loss rates, only the tidal streamers from the LMC would be detectable as local overdensities in star counts, though the debris from the other satellites might be found by integrating the star counts along the suspected orbital path (as proposed in JHB) or using additional color, kinematic, or distance information. These examples also imply that tidal streamers from such minor accretion events in external galaxies are likely to be unobservable.

3.2. *How Long Will We See a Satellite After Disruption?*

The central surface density of a remnant at time t after the destruction of a satellite is given by

$$\frac{\Sigma}{\Sigma_0} = m_{\rm sat} \frac{dN}{d\Psi} \frac{R_p}{r_{\rm tide}} \frac{1}{\Sigma_0} = \frac{1}{2d} \frac{1}{t\dot{\Psi}(t)} , \qquad (23)$$

where $\Sigma_0 = m_{\rm sat} R_p^2/r_{\rm tide}^2$ is the approximate surface density of the satellite as it disrupts. This is plotted in Figure 9 for a circular orbit (*heavy curve*) and orbits with eccentricities spanning the range $R_p/R_a = 0.07 - 1.0$, where R_a is the apocentric distance (as in Fig. 6). In all cases, Σ/Σ_0 oscillates between apocenter and pericenter but with a characteristic

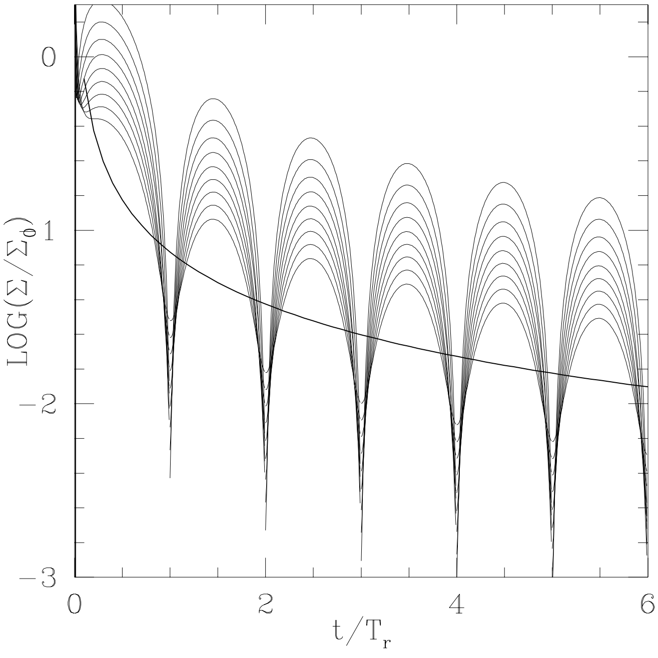

FIG. 9.—Evolution of the central surface density of a remnant following the complete destruction of a satellite for orbits with the same energy and eccentricities as in Fig. 6. Pericenter corresponds to the dip in each curve.

drop in amplitude by more than a factor of 10 within the first two radial periods ($\sim(2)^{1/2}T_\Psi$), which is in agreement with the results from Kroupa's (1997) simulations. For objects that have already been destroyed, we may take the surface densities of the dwarf spheroidals observed today (which are 10–100 times the background star counts—see Irwin & Hatzidimitriou 1995) as an upper limit to Σ_0. Then Figure 9 implies that local overdensities in star counts resulting from these disruption events would only be clear for the time period of the orbit (i.e., ~ 1 Gyr, see eq. [9]). However, the amplitude of the oscillation only decays linearly with time. This suggests that either a matched filtering technique, where star counts are integrated over some region (see, e.g., JHB), or a search including kinematic information could effectively find debris for the lifetime of the Galaxy (tens of orbital periods).

3.3. *How Lumpy is the Halo?*

We can estimate a timescale to characterize the rate of debris dispersal by calculating how long it will take the streamers from a satellite to extend 2π along its orbit:

$$\frac{T_{2\pi}}{T_\Psi} = \frac{\tau(2\epsilon)}{\tau(2\epsilon) - 1} = \frac{1}{1 - \exp\left(-\epsilon/v_h^2\right)}$$

$$= \frac{1}{1 - \exp\left[-(2Gm/R_p v_{\rm circ}^2)^{1/3}\right]} . \tag{24}$$

Figure 10 plots $T_{2\pi}/T_\Psi$ as a function of pericentric radius for various satellite masses and for each of the Milky Way's satellites (at either their pericentric or current positions for those with or without proper motion data, respectively). The upper axis shows T_Ψ for a circular orbit at radius R_p. The plot confirms the result of § 3.1 that debris from the LMC and Sagittarius is expected to spread more than 2π along their orbits over the lifetime of the Galaxy.

We can use this timescale to find the approximate angular length, L, of a streamer from a satellite that has lost mass during the last 10 Gyr:

$$L = \frac{10\ \mathrm{Gyr}}{T_\Psi} \frac{2\pi}{T_{2\pi}/T_\Psi} , \tag{25}$$

and this is included in Table 2. Combining this with the width of the streamer (eq. [17]) and approximating T_Ψ with the time period of a circular orbit at the pericentric position, we can estimate the sky coverage, $w \times L$, of debris from satellites of various masses and pericentric distances, as shown in Figure 11.

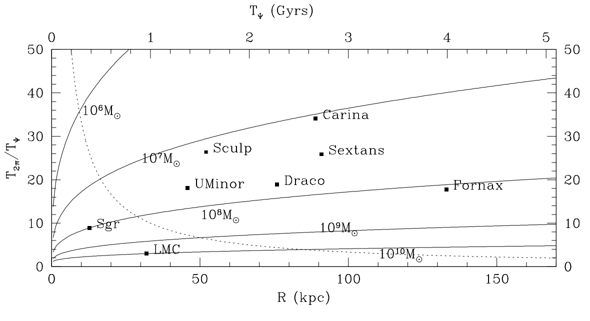

FIG. 10.—Time taken for debris to disperse over a full great circle (in units of the azimuthal time period of the orbit), as a function of distance and for a variety of satellite masses (*solid lines*). The dotted line is the curve $T_{2\pi} = 10$ Gyr. The Galactic satellites are plotted either at their current distance or their calculated pericentric distance (for those with proper motions). The equivalent time period for a circular orbit at each distance is shown along the top axis. For example, this plot implies that it will take $(T_{2\pi}/T_\Psi \sim 19) \times (T_\Psi \sim 2.3\ \mathrm{Gyr}) = 43.7$ Gyr for the tidal streamers from Draco to encircle the Galaxy.

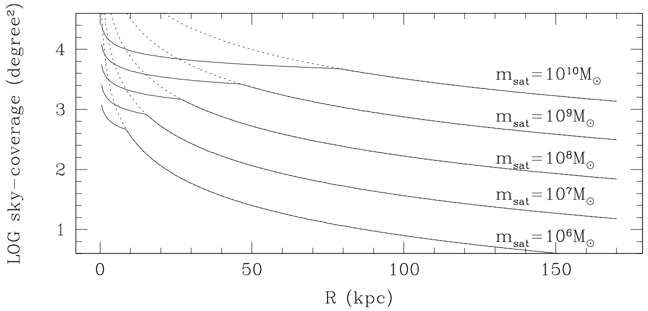

FIG. 11.—Each curve shows the fractional sky coverage of debris from a satellite of mass $m_{\rm sat}$ after 10 Gyr, as a function of its Galactocentric distance. The dotted lines show the behavior if the streamer is not assumed to overlap itself when it extends more than 2π along the satellite's orbit.

The lumpiness of halos with different accretion histories can be assessed by superimposing an ensemble of these trails and calculating how much of the sky they cover. We assume that $M_{\rm acc}$ of the mass of the halo has been accreted in the form of $M_{\rm acc}/m_{\rm sat}$ satellites of mass $m_{\rm sat}$ to form a density distribution that follows that of the stellar halo (where $\rho \propto r^{-3.5}$; see Freeman 1996). Then we integrate the sky coverage of each individual trail over the number density of accreted satellites to find the expected number of trails, $n_{\rm trails}$, intersecting any random line of sight (or, equivalently, how much of the sky is covered).

Figure 12 shows $n_{\rm trails}$ as a function of satellite mass for $M_{\rm acc} = 10^8, 10^9, 10^{10}$, and $10^{11}\ M_\odot$ (see also Tremaine 1993 for a simple—and elegant—version of this calculation). Of course, we know neither the accretion history of the Galaxy nor the primordial spectrum of satellite masses. However, semianalytic calculations suggest that many of the Galactic globular clusters will disrupt in the next Hubble time and that those we see today are the remnants of a much larger primordial population (see, e.g., Murali & Weinberg 1996; Gnedin & Ostriker 1997). From § 3.2, we would not expect to see trails from such disruption events for more than a few orbital periods in star counts alone. However, if we suppose that ~ 100 similar objects (with masses of 10^5–$10^6\ M_\odot$) have been accreted in the halo in the last Hubble time, then

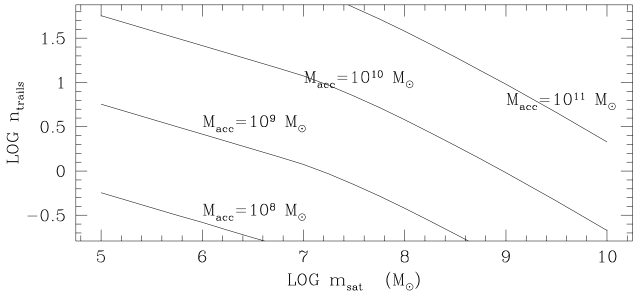

FIG. 12.—The curves show the number of trails observed along a random line of sight (or, equivalently, the fraction of the sky covered) for total accreted mass, $M_{\rm acc}$, as a function of the mass of the accreted satellites.

Figure 12 predicts that their debris trails would cover 10% of the sky. This significant sky coverage encourages the idea that many could be detected with kinematic surveys of halo stars along random lines of sight.

4. MICROLENSING IN A LUMPY HALO

In a recent paper, Zhao (1997) proposed several different scenarios in which the superposition of a debris trail between us and the Magellanic Clouds could explain all the microlensing events observed by the MACHO team (Alcock et al. 1996). Widrow & Dubinski (1997) found that such clumps were indeed occasionally "observed" in the dark matter searches that they conducted using a galaxy model extracted from a cosmological N-body simulation. Moreover, in a field 2° northwest of the LMC bar, Zaritsky & Lin (1998) find tantalizing evidence for such a foreground population of a suitable density and distance: 5% of the clump giants in their survey are 0.9 mag brighter than the mean. With the tools developed in this paper, we can reexamine the likelihood of each of Zhao's scenarios and hence the interpretation of Zaritsky & Lin's clump stars as tidal debris. (Note: the exact interpretation of this population and its contribution to the microlensing events has also been debated by several other authors; see Alcock et al. 1997, Gould 1997, Bennett 1997, and Beaulieu & Sackett 1997.)

In Zhao's (1997) first scenario, he assumes that the Magellanic plane (defined by the LMC and the Magellanic stream) is populated by a stream of debris, with lensing mass 10^{10} $M_\odot$, uniformly distributed along a great circle—equivalent to the model we discussed in § 3.1 for tidal streamers from the LMC. Our formalism predicts that the streamers would cover an area of 17 × 360 deg^2 (see Table 2). If the debris has the same mass-to-light ratio as the LMC, this would correspond to the luminosity of the entire stellar halo ($\sim 10^9$ $L_\odot$; see Freeman 1996) in only 10% of the sky and would produce an overdensity in star counts across the Magellanic Plane at high Galactic latitude of 10%–100% (see Fig. 8). It seems unlikely that such a significant population could have been missed in previous studies, since the number counts predicted by the Bahcall-Soneira model have been found to provide a reasonable fit to observations in all fields to which they have been applied (Bahcall 1986; Reid & Majewski 1993).

As an alternative, Zhao (1997) suggests debris just covering the extent of the clouds, either 10^{10} $M_\odot$ immediately in front of the clouds ($\sim$45 kpc from the Galactic center) or 10^8–10^9 $M_\odot$ at the Galactocentric distance of Sagittarius (16 kpc). In both cases, the timescale for such debris to disperse over an orbit is $\sim$3 Gyr (from the positions of the LMC and Sagittarius in Fig. 10), which suggests that such an alignment over just 10° would only last for less than 10^8 yr. Thus, this requires the destruction of an object of either mass within the last 10^8 yr and the alignment of its debris in just 1/400th of the sky. We conclude that, though not impossible, these scenarios are also unlikely.

5. SUMMARY AND DISCUSSION

We have outlined a method that can construct debris trails, using negligible computational resources, for any specified satellite mass and orbit and in most parent potentials, requiring only the assumption of a timescale over which the satellite is destroyed (see § 2.2).

The debris distributions generated by our approach demonstrate a remarkable agreement with those calculated from the positions of unbound particles at the end of simulations run in a fixed Galactic potential using equivalent satellite and orbit parameters (§ 2.2.3 and Fig. 5). This success encourages its use as a tool for understanding the evolution of tidal streamers from the accretion of small ($m_{\rm sat}/M_{\rm MW} < 1/100$) satellites after the potential fluctuations due to the initial formation of the Galaxy have died down and for which the limitations mentioned in the following paragraph do not apply.

The approximations inherent in this prescription (see § 2.3) imply that it is not well suited to generating debris distributions if the mass-loss rate is nearly constant (e.g., if the satellite is on a near circular orbit) or if the satellite's orbit is evolving because of dynamical friction with the parent galaxy. Both of these effects could conceivably be taken into account with a more sophisticated implementation of our technique. The method is clearly inapplicable to problems where the parent's potential is either triaxial or fluctuating as the result of a recent merger, such that the debris might be expected to diverge further from the satellite's orbit.

I thank R. van der Marel and J. Bahcall for invaluable comments on the manuscript, L. Hernquist and M. Bolte for the collaboration that provided the inspiration (and simulations) for this project, and S. Majewski for many useful discussions. The simulations used here were performed at the Pittsburgh Supercomputing Center. This work was supported by the Monell Foundation and the Institute for Advanced Study SNS Membership Fund.

APPENDIX

SIMULATIONS

The following is a brief sketch of the method and parameter ranges for the simulations, which are described fully in JHB.

In each simulation we represent the Milky Way by a rigid, three-component potential. The disk is described by a Miyamoto-Nagai potential (Miyamoto & Nagai 1975), the spheroid by a Hernquist (1990) potential, and the halo by a logarithmic potential:

$$\Phi_{\rm disk} = -\frac{GM_{\rm disk}}{\sqrt{R^2 + (a + \sqrt{z^2 + b^2})^2}}\,, \qquad \Phi_{\rm spher} = -\frac{GM_{\rm spher}}{r + c}\,, \qquad \Phi_{\rm halo} = v_{\rm halo}^2 \ln(r^2 + d^2)\,. \tag{A1}$$

We take $M_{\rm disk} = 1.0 \times 10^{11}$, $M_{\rm spher} = 3.4 \times 10^{10}$, $v_{\rm halo} = 128$, $a = 6.5$, $b = 0.26$, $c = 0.7$, and $d = 12.0$, where masses are in solar masses, velocities are in kilometers per second, and lengths are in kiloparsecs.

Each satellite is modeled with a collection of 10^4 self-gravitating particles, initially represented by a Plummer (1911) model:

$$\Phi = -\frac{Gm}{\sqrt{r^2 + r_0^2}}, \tag{A2}$$

where m is the mass of the satellite and r_0 is its scale length. During the simulations, the mutual interactions of the satellite particles are calculated using a self-consistent field code (Hernquist & Ostriker 1992), with the Milky Way's influence calculated from equation (A1).

In this paper, we consider the state of the satellite after 10 Gyr of evolution in twelve different simulations, whose parameters are outlined in Table 1. The first four models (1–4) have satellite and orbit parameters chosen at random to explore a range of possible outcomes. The remaining eight models all had the same orbit as model 2 but with satellite parameters chosen to change the rate of mass loss and debris dispersal. In models 5–8, the satellites have the same central density as model 2 but different velocity dispersions. In models 9–12, the satellites have the same velocity dispersion as model 2 but different central densities.

REFERENCES

Alard, C. 1996, ApJ, 458, L17
Alcock, C., et al. 1996, preprint (astro-ph/9606165)
———. 1997, preprint (astro-ph/9707310)
Arnold, R., & Gilmore, G. 1992, MNRAS, 257, 225
Bahcall, J. N. 1986, ARA&A, 24, 577
Bahcall, J. N., & Soneira, R. M. 1980, ApJS, 44, 73
Bennett, D. P. 1997, preprint (astro-ph/9710133)
Beaulieu, J. P., & Sackett, P. D. 1997, preprint (astro-ph/9710156)
Bergbusch, P. A., & VandenBerg, D. A. 1992, ApJS, 81, 163
Binney, J., & Tremaine, S. 1987, Galactic Dynamics (Princeton: Princeton Univ. Press)
Buonanno, R., Corsi, C. E., & Fusi Pecci, F. 1985, A&A, 145, 97
Da Costa, G. S., & Armandroff, T. E. 1995, AJ, 109, 2533
Eggen, O. J. 1965, in Galactic Structure, ed. A. Blaauw & M. Schmidt (Chicago: Univ. of Chicago Press), 111
Evans, C. R., & Kochanek, C. S. 1989, ApJ, 346, L13
Fahlman, G. G., Mandushev, G., Richer, H. B., Thompson, I. B., & Sivaramakrishnan, A. 1996, ApJ, 459, L65
Freeman, K. C. 1996, in ASP Conf. Ser. 92, The Formation of the Galactic Halo: Inside and Out, ed. H. Morrison & A. Sarajedini (San Francisco: ASP), 3
Fusi Pecci, F., Bellazzini, M., Cacciari, C., & Ferraro, F. R. 1995, AJ, 110, 1664
Gnedin, O., & Ostriker, J. P. 1997, ApJ, 474, 223
Gould, A. 1997, preprint (astro-ph/9709263)
Gould, A., Guhathakurta, P., Richstone, D., & Flynn, C. 1992, ApJ, 338, 345
Grillmair, C. J., Freeman, K. C., Irwin, M., & Quinn, P. J. 1995, AJ, 109, 2553
Hernquist, L. 1990, ApJ, 356, 359
Hernquist, L., & Ostriker, J. P. 1992, ApJ, 386, 375
Ibata, R. A., Gilmore, G., & Irwin, M. J. 1994, Nature, 370, 194
Ibata, R. A., Wyse, R. F. G., Gilmore, G., Irwin, M. J., & Suntzeff, N. B. 1997, AJ, 113, 634
Irwin, M. J., Bunclark, P. S., Bridgeland, M. T., & McMahon, R. G. 1990, MNRAS, 244, 16P
Irwin, M. J., & Hatzidimitriou, D. 1995, MNRAS, 277, 1354
Irwin, M., Ibata, R., Gilmore, G., Wyse, R., & Suntzeff, N. 1996, in ASP Conf. Ser. 92, The Formation of the Galactic Halo: Inside and Out, ed. H. Morrison & A. Sarajedini (San Fransisco: ASP), 84
Johnston, K. V., Hernquist, L., & Bolte, M. 1996, ApJ, 465, 278 (JHB)
Johnston, K. V., & Majewski, S. R. 1998, in preparation
Johnston, K. V., Spergel, D. N., & Hernquist, L. 1995, ApJ, 451, 598
Jones, B. F., Klemola, A. R., & Lin, D. N. C. 1994, AJ, 107, 1333
King, I. R. 1962, AJ, 67, 471
Klenya, J., Geller, M., Kenyon, S., & Kurtz, M. 1997, AJ, 113, 624
Kochanek, C. S. 1994, ApJ, 422, 508
Kroupa, P. 1997, New Astron., 2, 139
Kuhn, J. R., Smith, H. A., & Hawley, S. L. 1996, ApJ, 469, L93
Kunkel, W. E., & Demers, S. 1977, ApJ, 214, 21
Lin, D. N. C., & Richer, H. B. 1992, ApJ, 388, L57
Lynden-Bell, D. 1976, MNRAS, 174, 695
———. 1982, Observatory, 102, 202
Lynden-Bell, D. & Lynden-Bell, R. M. 1995, MNRAS, 275, 429
Maddox, S. J., Sutherland, W. J., Efstathiou, G., & Loveday, J. 1990, MNRAS, 243, 692
Majewski, S. R. 1994, ApJ, 431, L17
Majewski, S. R., Hawley, S. L., & Munn, J. A. 1996, in ASP Conf. Proc. 92, The Formation of the Galactic Halo: Inside and Out, ed. H. Morrison & A. Sarajedini, (San Francisco: ASP), 119
Majewski, S. R., Munn, J. A., & Hawley, S. L. 1994, ApJ, 427, L37
———. 1996, ApJ, 459, L73
Majewski, S. R., Phelps, R. L., & Rich, R. M. 1997, in ASP Conf. Ser. 112, The History of the Milky Way and its Satellite Systems, ed. A. Burkert, D. H. Hartmann & S. R. Majewski (San Francisco: ASP), in press
Mateo, M., Mirabel, N., Udalski, A., Szymański, M., Kubiak, M., Krzemiński, W., & Stanek, K. Z. 1996, ApJ, 458, L13
Mateo, M., Olszewski, E. W., Pryor, C., Welch, D. L., & Fischer, P. 1993, AJ, 105, 510
McGlynn, T. A. 1990, ApJ, 348, 515
Metcalf, B., & Silk, J. 1996, ApJ, 464, 218
Mighell, K. 1990, A&AS, 82, 207
Miyamoto, M., & Nagai, R. 1975, PASJ, 27, 533
Moore, B., & Davis, M. 1994, MNRAS, 270, 209
Murali, C., & Weinberg, M. D. 1996, astro-ph/9610229
Oh, K. S., Lin, D. N. C., & Aarseth, S. J. 1995, ApJ, 442, 142
Pennington, R. C., Humphreys, R. M., Odewahn, S. C., Zumach, W., & Thurmes, P. M. 1993, PASP, 105, 521
Piatek, S., & Pryor, C. 1995, AJ, 109, 1071
Plummer, H. C. 1911, MNRAS, 71, 460
Reid, N., & Majewski, S. R. 1993, ApJ, 409, 635
Roche, E. A. 1847, Academie des Sciences et Lettres de Montpellier, Memoirs de la Section des Sciences, Vol. 1, 243
Sackett, P. D. 1997, ApJ, 483, 103
Schweitzer, A. E., Cudworth, K. M., & Majewski, S. R. 1998, AJ, submitted
Schweitzer, A. E., Cudworth, K. M., Majewski, S. R., & Suntzeff, N. B. 1995, AJ, 110, 2747
Sommer-Larsen, J., & Christiansen, P. R. 1987, MNRAS, 225, 499
Sridhar, S., & Tremaine, S. 1992, Icarus, 95, 86
Tremaine, S. 1993, in AIP Conf. Proc. 278, Back to the Galaxy, ed. S. S. Holt & F. Verter (New York: AIP), 599
Unavane, M., Wyse, R. F. G., & Gilmore, G. 1996, MNRAS, 278, 727
Velazquez, H., & White, S. D. 1995, MNRAS, 275, L23
Walker, A. R. 1992, ApJ, 390, L81
Widrow, L. M., & Dubinski, J. 1997, astro-ph/9709220
Weir, N., Fayyad, U. M., & Djorgovski, S. G. 1995, AJ, 109, 2401
Zaritsky, D., & Lin, D. N. C. 1998, ApJ, in press
Zhao, H. S. 1997, preprint (astro-ph/9703097)